

Uncovering fossils of the distant Milky Way with UNIONS: NGC 5466 and its stellar stream

Jaclyn Jensen^{1*}, Guillaume Thomas^{2,3,4}, Alan W. McConnachie^{4,1}, Else Starckenburg⁵, Khyati Malhan⁶, Julio Navarro¹, Nicolas Martin⁷, Benoit Famaey⁷, Rodrigo Ibata⁷, Scott Chapman⁸, Jean-Charles Cuillandre⁹, Stephen Gwyn⁴

¹*Department of Physics & Astronomy, University of Victoria, Victoria, BC, V8P 1A1, Canada*

²*Instituto de Astrofísica de Canarias, E-38205 La Laguna, Tenerife, Spain*

³*Universidad de La Laguna, Dpto. Astrofísica, E-38206 La Laguna, Tenerife, Spain*

⁴*NRC Herzberg Astronomy & Astrophysics, 5071 West Saanich Road, Victoria, BC, V9E 2E7, Canada*

⁵*Kapteyn Astronomical Institute, University of Groningen, Landleven 12, 9747 AD Groningen, The Netherlands*

⁶*The Oskar Klein Centre for Cosmoparticle Physics, Department of Physics, Stockholm University, AlbaNova, 10691 Stockholm, Sweden*

⁷*l'Université de Strasbourg, CNRS, Observatoire astronomique de Strasbourg, UMR 7550, F-67000 Strasbourg, France*

⁸*Department of Physics and Atmospheric Science, Dalhousie University, 6310 Coburg Rd., Halifax, NS B3H 4R2 Canada*

⁹*AIM, CEA, CNRS, Université Paris-Saclay, Université Paris Diderot, Sorbonne Paris Cité, Observatoire de Paris, PSL University, F-91191 Gif-sur-Yvette, France*

Accepted 2021 August 6; Received 2021 July 15; in original form 2021 June 2

ABSTRACT

We examine the spatial clustering of blue horizontal branch (BHB) stars from the u -band of the Canada-France Imaging Survey (CFIS, a component of the Ultraviolet Near-Infrared Optical Northern Survey, or UNIONS). All major groupings of stars are associated with previously known satellites, and among these is NGC 5466, a distant (16 kpc) globular cluster. NGC 5466 reportedly possesses a long stellar stream, although no individual members of the stream have previously been identified. Using both BHBs and more numerous red giant branch stars cross-matched to *Gaia* Data Release 2, we identify extended tidal tails from NGC 5466 that are both spatially and kinematically coherent. Interestingly, we find that this stream does not follow the same path as the previous detection at large distances from the cluster. We trace the stream across 31° of sky and show that it exhibits a very strong distance gradient ranging from $10 < R_{\text{helio}} < 30$ kpc. We compare our observations to simple dynamical models of the stream and find that they are able to broadly reproduce the overall path and kinematics. The fact that NGC 5466 is so distant, traces a wide range of Galactic distances, has an identified progenitor, and appears to have recently had an interaction with the Galaxy's disk, makes it a unique test-case for dynamical modelling of the Milky Way.

Key words: globular clusters: individual: NGC 5466 – Galaxy: kinematics and dynamics – Galaxy: halo – Galaxy: structure

1 INTRODUCTION

In the standard Λ CDM cosmology, galaxies form hierarchically via a series of mergers (White & Rees 1978; Johnston et al. 2008). Larger galaxies accrete smaller stellar systems together with their own globular clusters, and tidal forces act to strip stars from these satellites to form stellar streams. At large distances from the Galaxy's center, dynamical timescales are long such that signatures of these mergers may be observable for many billions of years (Johnston et al. 1996)

and form part of the Galaxy's "fossil record". In particular, kinematics and chemical abundances of old stars in these streams provide key insights into the merger history of the Milky Way and the formation of the "proto-Galactic fragments" that have since merged (Searle & Zinn 1978).

In recent years, revolutionary large-sky surveys have provided unprecedented perspectives of the Milky Way – for example, the Sloan Digital Sky Survey (SDSS; York et al. 2000), Pan-STARRS1 3π survey (PS1 3π ; Chambers et al. 2016), and the Dark Energy Survey (DES; The Dark Energy Survey Collaboration 2005) to name a few. Most notably, the advent of *Gaia* (Gaia Collaboration

* E-mail: jaclynjensen@uvic.ca

et al. 2016) has been instrumental to measuring the positions and proper motions for billions of stars and developing a detailed map of our Milky Way. *Gaia*'s second data release (*Gaia* DR2; [Gaia Collaboration et al. 2018](#)) ignited a prosperous era for Galactic archaeology, with a host of newly identified substructures. Some key studies using *Gaia* DR2 include (1) searches for stellar streams ([Malhan et al. 2018](#); [Mateu et al. 2018](#); [Ibata et al. 2019](#); [Necib et al. 2020](#); [Borsato et al. 2020](#)), (2) updated globular cluster kinematics ([Baumgardt et al. 2019](#)) (3) identification of tidal tails from globular clusters ([Bianchini et al. 2019](#); [Kundu et al. 2019](#); [Sollima 2020](#); [Thomas et al. 2020](#)), (4) new estimates for the Milky Way mass profile ([Cautun et al. 2020](#)), and (5) unveiling the Galaxy's complex accretion history ([Helmi et al. 2018](#); [Mackereth et al. 2019](#)), among many other advancements.

Streams around globular clusters have proven to be powerful probes of the Galactic potential (e.g., [Küpper et al. 2015](#); [Pearson et al. 2015](#); [Thomas et al. 2017, 2018b](#); [Bonaca & Hogg 2018](#); [Malhan & Ibata 2019](#)). Due to their lower initial masses and velocity dispersions, globular cluster streams are typically thin, dynamically cold, and extremely sensitive to perturbations from the host potential. Each substructure represents a unique interaction with the Galaxy, yet few are known at large (> 10 kpc) distances. Increasing the number of known systems in this regime, especially those with clear progenitors, can place tighter constraints on the shape and mass of the dark matter halo interior to each distant stream's orbit.

Gaia's precise astrometry has provided many of the pieces necessary to better understand the Galaxy's interactions with its satellites. However, parallax uncertainties of fainter sources are much less accurate at large distances ([Lindegren et al. 2018](#)); therefore, exploring the distant Milky Way with *Gaia* alone is difficult. In contrast, *Gaia* proper motions remain extremely useful even deep into the stellar halo ([Powell 2013](#); also see Figure 1 in [Ibata et al. 2017b](#)).

To push *Gaia* out to the distant Galaxy, we have estimated photometric parallaxes of tracer stellar populations using *u*-band data from the Canada-France Imaging Survey (CFIS; [Ibata et al. 2017a](#)) combined with *Gaia* *G*- ([Gaia Collaboration et al. 2018](#)) and PS1 3π *griz*-bands ([Chambers et al. 2016](#)). At these larger distances, estimated photometric parallaxes based on high-quality ground-based photometry can be very accurate (see the seminal study of [Jurić et al. 2008](#)). In [Thomas et al. \(2018a, 2019\)](#) we show that we can obtain distances for stellar populations in the stellar halo (> 10 kpc) that are considerably more accurate than *Gaia* alone. In combination with *Gaia* proper motions, we can therefore explore the dynamical structure of the stellar halo to larger distances than would be otherwise possible.

The paper is organized as follows. In Section 2 we discuss the various large-sky surveys and preliminary data processing of the CFIS tracer populations used in this work. Section 3 details our method to probe the halo via a clustering algorithm that visualizes the hierarchical nature of halo substructures. Analysis of the major features leads us to identify a putative stellar stream around NGC 5466, which forms the focus of the remainder of the paper due to its interesting yet ill-defined properties. We quantify these properties in Section 4, and in Section 5, we conduct simple dynamical modelling of this stellar stream. We compare our model to the observational data and previous work in Section 6, and summarize our results in Section 7.

2 PRELIMINARIES

2.1 CFIS, UNIONS, and *Gaia*

CFIS is an on-going Large Program using the MegaCam imager ([Boulade et al. 2003](#)) at the Canada-France Hawaii Telescope (CFHT). When completed, the survey will have ground-based *u*- and *r*-band photometry for 10,000 and 5,000 deg² of the northern sky, respectively. The primary motivation for the extensive CFIS-*u* imaging is its power for Galactic studies of nearby stellar populations, in addition to its complementarity to the *Euclid* mission ([Laureijs et al. 2011](#); [Racca et al. 2016](#)). As demonstrated in [Ibata et al. \(2017a\)](#) (see their Figure 5), the CFIS *u*-band is deeper than SDSS by ~ 2.7 magnitudes as a result of longer integration times on a larger telescope, which is much more optimized for UV by design (e.g., optical coatings) compared to other facilities. CFIS is focused at Galactic latitudes of $|b| > 19^\circ$ and is well-suited for studying the halo. Figure 1 shows the final overall footprint of the CFIS-*u* component in blue, where the red regions are the area currently available in this work.

Recently, the scope of CFIS has expanded alongside multiple other northern hemisphere imaging surveys. Specifically, the Ultraviolet Near-Infrared Optical Northern Survey (UNIONS) is a new consortium of wide-field imaging surveys of the northern hemisphere. UNIONS consists of the CFIS team, members from Pan-STARRS, and the Wide Imaging with Subaru HyperSuprime-Cam of the Euclid Sky (WISHES) team. Each group is currently collecting imaging at their respective telescopes: CFHT/CFIS is targeting deep *u*- and *r*-band photometry, Pan-STARRS is obtaining deep *i*- and moderate-deep *z*-bands, and Subaru/WISHES is acquiring deep *z*. These independent efforts are directed, in part, to securing optical imaging to complement the *Euclid* space mission, although UNIONS is a separate consortium aimed at maximizing the science return of these large and deep ground-based surveys of the northern skies.

In this contribution, we make use of the UNIONS/CFIS *u*-band data only. All CFIS-*u* sources used in this work are cross-matched to the *griz*-bands of the PS1 3π survey for complete photometric coverage across the optical spectrum (note that PS1 3π should not be confused with the new Pan-STARRS *i*- and *z*-band imaging being obtained as part of the UNIONS effort). Astrometry for these sources are obtained from the second *Gaia* data release ([Gaia Collaboration et al. 2018](#)), as this work preceded the arrival of *Gaia* eDR3 ([Gaia Collaboration et al. 2020](#)).

2.2 Tracer stellar populations

The *u*-band is exceptionally useful for the study of nearby stellar populations. For example, a star's absolute magnitude is sensitive to its metallicity, and many metal lines are found in the UV-blue region of the spectrum. This fact is particularly useful to photometrically identify target populations and derive basic parameters. In this work, we target specific tracer stellar populations for which the absolute magnitudes are reasonably well-constrained. The resulting distances, when paired with the excellent proper motions from *Gaia* DR2, gives us a more complete kinematic view of the outer Galaxy than is possible when using solely *Gaia*.

The first stellar population used in this study are the blue horizontal branch stars (BHBs) that were identified in [Thomas et al. \(2018a, hereafter T18\)](#). BHBs are an ideal tracer to probe the stellar halo for substructure: these bright A-type giants have relatively stable absolute magnitudes ($M_g \sim 0.5 - 0.7$ mag; [Deason et al.](#)

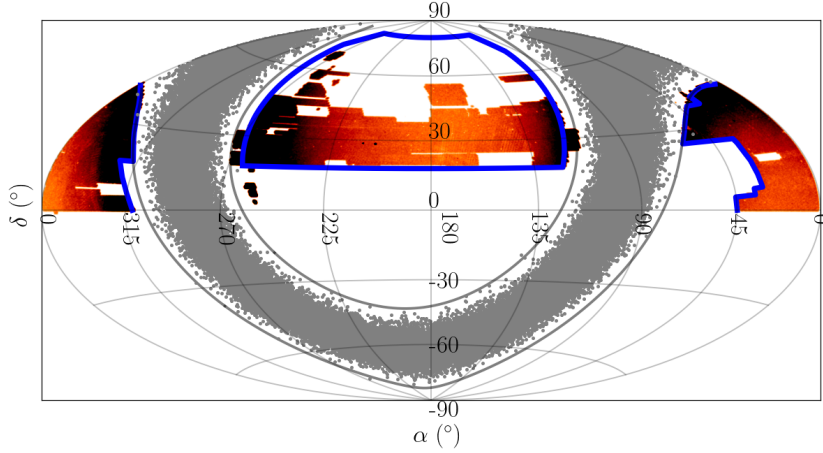


Figure 1. CFIS-*u* equatorial footprint. Blue outlines show the final CFIS area when the survey is complete ($\sim 5,000 \text{ deg}^2$), while red/orange shaded regions are the fields available at the time of the current study ($\sim 4,000 \text{ deg}^2$). Grey solid lines are located at $b = \pm 20^\circ$ to highlight the boundary of CFIS in Galactic latitude; grey points in this area highlight the approximate position of stars in the disk.

2011), allowing us to trace them out to large distances. Using CFIS-*u* and PS1-*griz* extinction-corrected bands, T18 identified A-type stars using a sequence of color-color cuts. BHB stars were then disentangled from contaminating blue stragglers via a random forest classifier, producing a sample of $\sim 10,200$ BHBs with $\sim 25\%$ contamination from blue straggler stars. The absolute magnitudes were derived using the calibration from Deason et al. (2011), where M_g is a function of $(g_0 - r_0)$. In T18, the heliocentric (photometric) distances are estimated from M_g which are shown to be accurate to $\sim 10\%$, extending out to $\sim 220 \text{ kpc}$.

The second tracer population used in this work is from the catalog of “dwarfs” and “giants” in Thomas et al. (2019, hereafter T19). Briefly, T19 implemented a machine learning scheme to classify stars as either main sequence (MS/“dwarfs”) or red giant branch (RGB/“giants”), using SEGUE spectra and *Gaia* photometry and parallaxes as a training set. For both the dwarfs and the giants, photometric metallicities ($[\text{Fe}/\text{H}]$) and absolute magnitudes in *Gaia* *G*-band (M_G) were estimated. The initial classification assigns a probability to each star that it is either a dwarf or giant (such that $P_{\text{dwarf}} + P_{\text{giant}} = 1$) based on its color using the combined photometry of CFIS-PS13 π -*Gaia* *G*. The algorithm successfully identifies 70% of metal-poor giants with $[\text{Fe}/\text{H}] < -1.2 \text{ dex}$. Then, each population is run through their own set of Artificial Neural Networks, which serve to estimate $[\text{Fe}/\text{H}]$ and M_G from the training set. T19 show that the uncertainties on the photometric metallicities and distances for the giants are approximately 0.3 dex and $< 25\%$, respectively. These authors also note that more metal-rich giants are often misidentified, resulting in a significant drop in completeness for $[\text{Fe}/\text{H}] > -1 \text{ dex}$. This minimally affects our current study, as we are primarily concerned with giants in the metal-poor regime.

In what follows, we start with a dataset composed of all likely giants (those with $P_{\text{giant}} > 50\%$; of order $\sim 600,000$ sources). We then remove any potential background galaxies using the PS1 criterion in Farrow et al. (2014), $|r_{\text{PSF}} - r_{\text{ap}}| < 0.05$. While this method becomes unreliable for stars fainter than $r_{\text{PSF}} > 21 \text{ mag}$, 99.9% of stars in this dataset are brighter than this limit – given that we are limited by the depth of *Gaia* at $G \approx 21 \text{ mag}$. As discussed, an artefact of the method of T19 is the misidentification of more metal-rich stars. Following their recommendations, we remove this

contamination by restricting the uncertainties of the predicted absolute magnitudes, $\delta M_{G,\text{pred}} \leq 0.5 \text{ mag}$ (where $\delta M_{G,\text{pred}}$ includes the photometric and systematic errors added in quadrature). This reduces our sample size to $\sim 201,000$ RGBs. Finally, we apply a restriction to the *Gaia* parallaxes, in order to avoid nearby stars in the Solar neighborhood (Lindegren et al. 2018). This equates to a parallax cut at $> 0.2 \text{ mas}$, or equivalently, removing stars whose heliocentric distances are less than 5 kpc. Gaia Collaboration et al. (2018) also recommend a zero-point correction of -0.03 mas to account for the global parallax offset. Therefore, we adopt:

$$\frac{1}{\pi + 0.03 \text{ mas}} > 5 \text{ kpc} \quad (1)$$

This provides us with a total sample of $\sim 103,000$ RGB stars with positions, proper motions, distances, and metallicities.

3 SEARCHING THE HALO FOR STELLAR SUBSTRUCTURES

In this section, we begin by examining the clustering of the outer halo, taking advantage of the relatively precise distances of the BHB sample. We identify several major substructures, all of which are well-known, including the NGC 5466 globular cluster. We identify a group of co-moving stars surrounding NGC 5466 and attempt to better trace its extension using improved statistics (but less precise distances) of the T19 RGBs.

3.1 Examining the clustering of blue horizontal branch stars

3.1.1 The OPTICS spatial clustering algorithm

The identification of halo substructures within the spatial distribution of stars requires an algorithm that can identify the clustering of points without strong restrictions on the range of allowable sizes and shapes, and which ideally allows for hierarchical distributions (i.e., substructures within substructures). Here, we opt to use the density-based algorithm known as OPTICS (Ordering Points to Identify Clustering Structure; Ankerst et al. 1999).

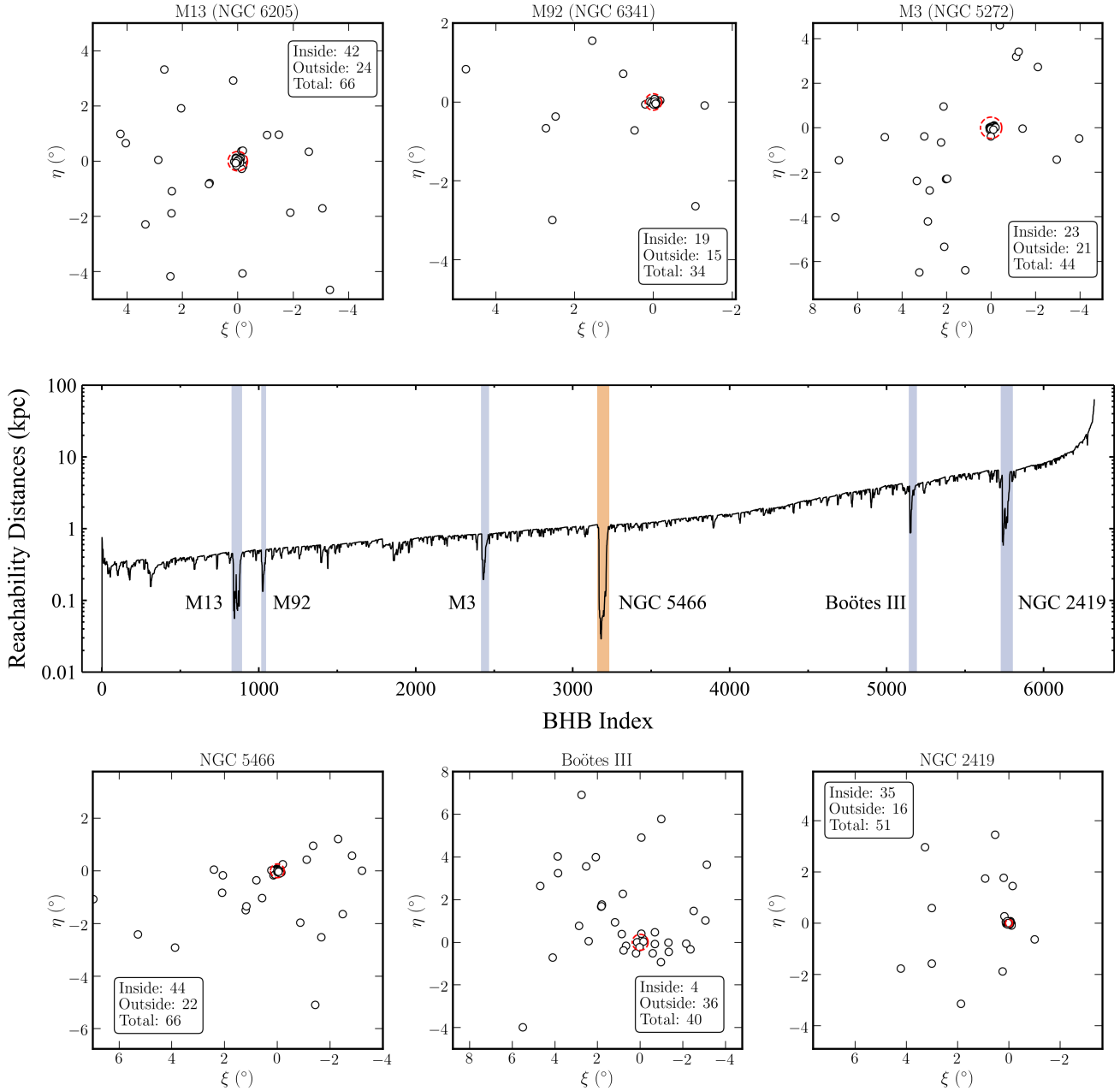


Figure 2. The dendrogram produced by OPTICS (central panel) with major substructures highlighted. Top and bottom rows show the tangent plane projection of the stars associated with each of these substructures, which correspond to known globular clusters or dwarf galaxies. For each, the red dashed circle corresponds to the literature measurement of the cluster’s tidal radius (or in the case of Boötes III, its half-light radius). Statistics for each object are listed describing the number of BHBs inside and outside r_t (or r_h).

OPTICS is similar in methodology to other connectivity-based clustering algorithms such as DBSCAN (Ester et al. 1996). However, OPTICS is more optimal for our study as it does not (a) automatically segregate the data into clusters, (b) requires only one user-specified parameter (N_{min} , the minimum number of points that can define a substructure) further limiting potential biases imparted by the algorithm, and (c) produces a useful dendrogram for visualizing the clustering within a dataset (known as the “Reachability Diagram”). OPTICS works by reordering data such that points in the same neighborhood are physically close together in the dendrogram.

Overdensities in this plot stand out as “valleys”, or neighborhoods in which the density is clearly higher than its surroundings.

The application of OPTICS to astronomical datasets is, to the best of our knowledge, relatively new. It has been tested with simulations of the Milky Way stellar halo (Sans Fuentes et al. 2017), and has been applied to quantify the properties of the halo of M31 (McConnachie et al. 2018). Most recently, Oliver et al. (2020) examine in detail how to best apply OPTICS to the study of stellar halos. We refer to these papers for complete details on OPTICS.

3.1.2 Identifying the most prominent substructures

First, we transform all BHB positions to the Galactocentric frame using their photometric distances and equatorial positions. For this calculation, we assume the Sun’s position is $(X, Y, Z)_{\odot} = (-8.122, 0, 0.025)$ kpc (Gravity Collaboration et al. 2019; Jurić et al. 2008). Then, for stars in the northern Galactic region ($b > 20^{\circ}$; between R.A. = $[270^{\circ}, 90^{\circ}]$ of Figure 1), we apply OPTICS to their (X, Y, Z) Galactocentric positions, assuming the minimum number of points to classify a substructure is $N_{min} \geq 6$. We choose this value for N_{min} as it is sufficient to identify known structures such as globular clusters without producing much noise in the Reachability Diagram.

The resulting Reachability Diagram is shown in the central panel of Figure 2. The x-axis represents the order, or index, of the BHBs within the reorganized dataset. As a result, points physically located near other points in a neighborhood appear close together on the x-axis.

The y-axis of Figure 2 shows the reachability-distances (RDs) for each star, or the physical distance of a BHB to its associated cluster. RDs essentially give an estimate for the spatial scale of each neighborhood, where clusters in the dataset are represented as valleys. These structures show stars that have small RDs compared to their background, and therefore can be considered a substructure relative to their surroundings.

OPTICS does not automatically define clusters, so we use a custom algorithm also used in McConnachie et al. (2018) to identify prominent valleys. The most significant structures identified with this algorithm are highlighted in Figure 2, also corresponding to the largest features identifiable by eye. Of these six highlighted valleys, five are associated to known globular clusters (Harris 1996, 2010 edition) and one to a tidally disrupting dwarf galaxy (Boötes III; Grillmair & Carlin 2016). The surrounding panels of Figure 2 show tangent-plane projections of the member stars in each feature, centered on each satellite’s position. We show the King tidal radii (r_t ; Moreno et al. 2014) in each panel as a red dashed circle; Boötes III is the only exception where we instead show the half-light radius measured by Carlin et al. (2009). In each case, a significant number of BHBs identified as being associated to the main structure lie well beyond the tidal radii of the satellite. If any of these OPTICS-identified stars are indeed actually associated with the satellite, this would suggest extended features around each object.

Below, we briefly summarize the literature associated with each satellite including any previous detections of tidal debris:

- M 13 (NGC 6205) was found to have a “halo of unbound stars” by Lehmann & Scholz (1997) who first examined its King profile (King 1962) and identified a surface density excess at the outer regions of the cluster. Later, Leon et al. (2000) similarly found an extension of stars towards the Galactic center; however, these stars all lie within the cluster’s estimated tidal radius.
- Tidal tails from the M 92 cluster (NGC 6341) have recently been discovered in two separate detections by Sollima (2020) and Thomas et al. (2020), with the latter paper identifying lengthy tails extending over $\sim 17^{\circ}$.
- Two papers (Leon et al. 2000; Grillmair & Johnson 2006) searched for stripping surrounding the M 3 globular cluster (NGC 5272) but do not find any evidence of disruption.
- NGC 2419 is a cluster which likely originated from the Sagittarius dwarf galaxy (Bellazzini et al. 2020). At a distance of ~ 83 kpc (Harris 1996, 2010 edition), the current tidal forces experienced by this cluster will be quite weak, and no tails have previously been reported.

Table 1. Observational properties of NGC 5466 summarized from the literature. (1) Harris (1996, 2010 edition), (2) Moreno et al. (2014), (3) Pryor et al. (1991); Fellhauer et al. (2007), (4) Baumgardt et al. (2019).

Parameter	Value	Source
R.A. (α)	211.3637°	(1)
Dec. (δ)	28.5344°	
Distance (R_{helio})	16.0 ± 0.4 kpc	
Concentration (c)	1.04 ± 0.2	
Half-light radius (r_h)	$2.3 \pm 0.07'$	
Core radius (r_c)	$1.43 \pm 0.1'$	
Metallicity ($[Fe/H]$)	-1.98 ± 0.09 dex	
King tidal radius (r_t)	72.98 pc	(2)
Stellar mass	$\sim 5 \times 10^4 M_{\odot}$	(3)
Proper motion in R.A. (μ_{α}^*)	-5.41 ± 0.01 mas yr $^{-1}$	(4)
Proper motion in Dec. (μ_{δ})	-0.79 ± 0.01 mas yr $^{-1}$	
Radial Velocity (v_r)	106.93 ± 0.18 km s $^{-1}$	

- The Boötes III dwarf galaxy is currently being tidally disrupted, and is likely the progenitor of the Styx stellar stream (Grillmair 2009; Carlin et al. 2009; Carlin & Sand 2018).

- Evidence for mass loss from the NGC 5466 globular cluster was first presented in Pryor et al. (1991) and Lehmann & Scholz (1997). Two detections of tidal tails from this cluster were observed in SDSS, but differed in length: Belokurov et al. (2006) identified extra-tidal stars out to 4° , while Grillmair & Johnson (2006) found very extended tails stretching over $\sim 45^{\circ}$ of sky using a matched filter method. Fellhauer et al. (2007) and Lux et al. (2012) modeled the disruption of the cluster based upon the Grillmair & Johnson (2006) detection. These dynamical studies were only able to reproduce the path of the tails over a segment of the matched filter map up to R.A. $\lesssim 192^{\circ}$.

The search for new Galactic structures in *Gaia* DR2 has been plentiful, and many groups have mined this catalogue for stellar streams; for example, Malhan et al. (2018) and Ibata et al. (2019) found 13 new streams using the STREAMFINDER algorithm applied to *Gaia* 5-D kinematics, Mateu et al. (2018) identified 14 candidate streams searching over great circles of RR Lyrae, and additional works identifying substructures were conducted by Helmi et al. (2017), Necib et al. (2019), Borsato et al. (2020) (to name a few others). During the final stages of preparation of this manuscript, Ibata et al. (2020) applied STREAMFINDER to *Gaia* eDR3 and identified some stars associated with a putative stream from NGC 5466 extending $\sim 18^{\circ}$ on the sky, although no follow-up or commentary was provided.

3.1.3 A closer look at NGC 5466

NGC 5466 is a relatively distant cluster ($R_{helio} = 16$ kpc). Therefore, a large stream from this satellite would constitute a valuable dynamical tracer of the gravitational potential for the distant Galaxy. A review of the literature to date on this satellite highlights some discrepant claims surrounding the putative stream’s properties, which has also proven difficult to model satisfactorily. The extensive coverage of CFIS therefore seems well-suited to better determine the

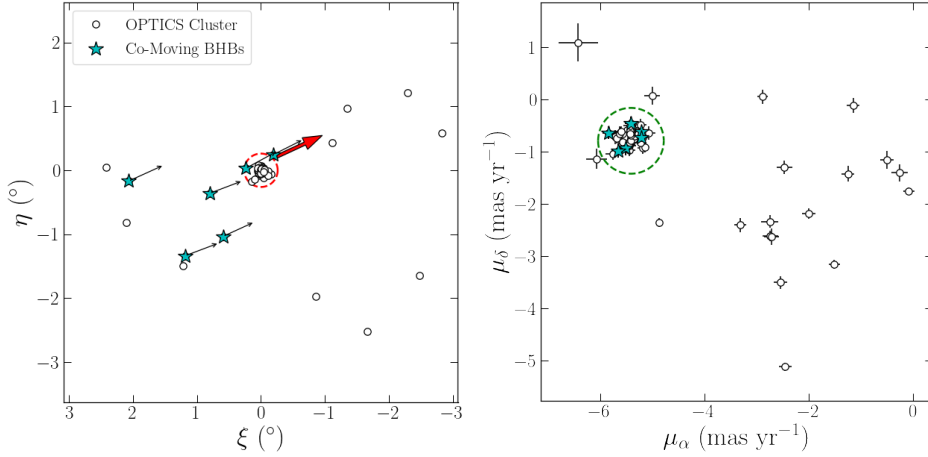


Figure 3. Left: Tangent plane projection of the OPTICS BHBs identified as part of the NGC 5466 group (orange valley in Figure 2). The red dashed circle corresponds to the tidal radius of the cluster, and the red arrow represents the proper motion of the cluster (Baumgardt et al. 2019) corrected for Solar reflex motion. Right: Proper motion vector point diagram for the OPTICS BHBs of NGC 5466. The cluster of stars within the green circle correspond to stars moving with the same systemic proper motion as the cluster. We highlight the BHBs corresponding to stars moving with the cluster (outside r_t) as cyan stars in both panels. Their (Solar reflex-corrected) proper motion vectors are also shown as black arrows in the tangent plane.

stream’s properties. It is with these considerations in mind that we decided to conduct a more complete examination of this structure. We summarize the relevant observational parameters of NGC 5466 in Table 1.

Figure 3 shows the resulting OPTICS grouping for NGC 5466. The left panel shows a zoom-in of the tangent plane as seen in Figure 2 and the right shows their associated proper motions and uncertainties as reported by *Gaia* DR2. Proper motion errors are corrected by a factor of 1.1, as these values are typically underestimated by 7 – 10% for fainter sources ($G > 16$ mag; Lindegren et al. 2018). The centroid of the green circle is located at the cluster’s proper motion $(\mu_\alpha^*, \mu_\delta) = (-5.41, -0.79)$ mas yr $^{-1}$ as derived by Baumgardt et al. (2019). We also represent the cluster’s motion in the tangent plane as the red vector, after correcting for Solar reflex motion assuming a distance to the cluster of 16.0 kpc (Harris 1996, 2010 edition). For this calculation, we adopt Local Standard of Rest (LSR) values from Schönrich et al. (2010) $(U, V, W)_\odot = [11.1, 12.24, 7.25]$ km s $^{-1}$ assuming the circular velocity at the Sun is 229 km s $^{-1}$ (Eilers et al. 2019) and the Sun’s position is the same as in Section 3.1.2.

The right panel of Figure 3 shows a clear clustering of points corresponding to the systemic proper motions of NGC 5466. Interestingly, there are six BHBs outside r_t (red dashed circle) whose proper motions are consistent with stars in the cluster’s main body, shown in both panels as the cyan stars. As done previously with the cluster’s proper motion vector, we correct these cyan stars for Solar reflex motion using their photometric distances and previously assumed values for the motion and position of the Sun. We overlay their corrected proper motion vectors on the tangent plane to show these BHBs are clearly moving in a similar fashion as the globular cluster itself, suggesting they are an extra-tidal population from NGC 5466. Our detection of a co-moving group of BHBs is consistent with earlier findings of the stream from Belokurov et al. (2006) and Grillmair & Johnson (2006). However, the BHB population by itself is too sparse to clearly define the path of this putative stream.

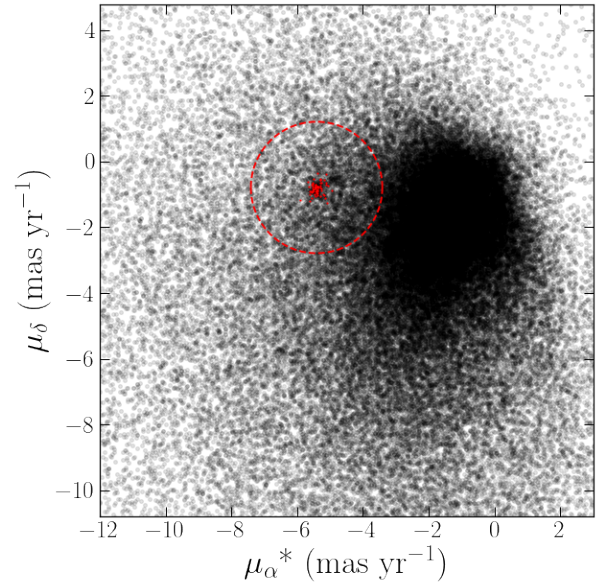


Figure 4. Vector point diagram of all giants ($P_{\text{giant}} > 50\%$) in the CFIS dataset. Stars within $1 - 2r_h$ of the cluster are shown as red points. The red dashed circle is the 2 mas yr $^{-1}$ boundary chosen to select stars with broadly similar proper motions to the globular cluster.

3.2 Using red giant branch stars to trace NGC 5466

3.2.1 Filtering the red giant branch stars

Here, we use the more numerous RGB stars to better trace the extended NGC 5466 system. We begin with the sample selected in Section 2.2 of $\sim 103,000$ stars, and first perform a simple cut in proper motion-space to remove obvious non-members. Figure 4 shows the vector point diagram of all RGBs in the current sample. Red points in this figure show stars within $1 - 2$ half-light radii (r_h) of NGC 5466, which form a tight clumping around the systemic proper motion of the cluster. We remove a large fraction of background contamination by only retaining stars whose proper motions

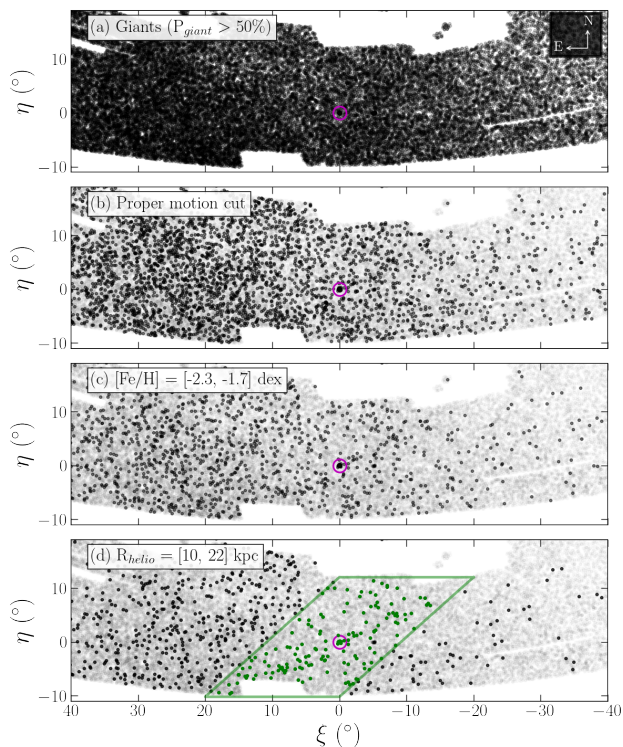


Figure 5. Tangent plane projection of giants in CFIS, centered on NGC 5466 (magenta circle). **(a):** Giants with $P_{\text{giant}} > 50\%$. **(b):** Grey points are the full sample as shown in (a), black points are the sample after filtering for proper motion. **(c):** Stars remaining after filtering for metallicity, $[\text{Fe}/\text{H}] = [-2.3, -1.7]$ dex. **(d):** Stars remaining after filtering for distance, $R_{\text{helio}} = [10, 22]$ kpc. Data within the green area are retained for further analysis.

fall within a 2 mas yr^{-1} radius around the mean value for the cluster (red dashed circle). This radius is nearly 10 times larger than the average proper motion uncertainties of stars in the cluster’s core, and is therefore unlikely to remove any stars associated to the cluster. This cut greatly reduces the sample down to $\sim 6,600$ stars. The top panel in Figure 5 shows the tangent plane for all giants in the original dataset, while the second panel shows the RGBs remaining after the proper motion cut.

NGC 5466 has a metallicity of $[\text{Fe}/\text{H}] \simeq -2$ dex (Harris 1996, 2010 edition) and no reported evidence of a spread in iron. Therefore, we require the metallicity for candidate stream members to be limited to a range of $[\text{Fe}/\text{H}] = [-2.3, -1.7]$ dex. The range is set by the global uncertainty on the metallicity of the giants in our dataset (± 0.3 dex; see T19). The stars that remain after this cut are shown in the third panel of Figure 5.

Finally, we restricted the allowable heliocentric distance range for the RGB stars. This selection was made primarily based on two factors: firstly, NGC 5466 is located 16 kpc away, and secondly, typical distance uncertainties for our stars are $\sim 25\%$. Further, the distance of stars along the stream are as of yet, unknown. It is quite possible that the putative stream may exhibit a significant distance gradient. For these reasons, we require $R_{\text{helio}} = [10, 22]$ kpc. The remaining stars in our dataset are shown in the lower panel of Figure 5.

3.2.2 Identifying stream members

The descending panels of Figure 5 show tentative evidence of an extended structure south-east and north-west of NGC 5466. If this structure is real, then there should be a gradient in the proper motions of the relevant stars seen on-sky, i.e. a coherent phase-space structure. To investigate this possibility, we selected stars within a generous polygon defined by the green box in panel (d) of Figure 5. This selection is made to broadly cover the area of the putative stream, without being too restrictive. We then automatically search for any stars that are consistent with displaying a gradient in their proper motions. Specifically:

- (i) We first examine the behaviour of μ_{α}^* as a function of α for all stars. We fit a straight line to all the data, where the weights are given by the uncertainties in the individual proper motions;
- (ii) We retain those stars that are less than 3σ from the fitted line. We then generate a new fit to these data;
- (iii) Using the fit from the previous step, we compare this fit to all the data (i.e. including stars that were rejected in the previous iteration), again only retaining stars less than 3σ from the fitted line.
- (iv) We repeat step (iii) until convergence;
- (v) For the stars that survive the sigma-clipping in μ_{α}^* vs α , we repeat the process for μ_{δ} vs δ .

Figure 6 shows the impact of applying this procedure to the dataset. Red points in this figure are the surviving members of the sigma-clipping. It is notable that these form a clear, coherent, and extended stream-like structure on the sky as shown in the right panel, with only a few outliers. We note that we have repeated this analysis for different polygon shapes of the selection box in panel (d) of Figure 5, and we have verified that our conclusions are independent of the exact shape of the polygon. We conclude that the red data shown in Figure 6 are a real detection of stars belonging to an extended stellar stream from NGC 5466. In what follows, we refer to these stars (beyond the tidal radius of NGC 5466) as our “gold” sample, and we additionally include the extra-tidal BHBs identified in Section 3.1.3. Properties of these stars are provided in Table 2.

4 QUANTIFYING THE PROPERTIES OF THE STELLAR STREAM FROM NGC 5466

In this section, we use the gold sample to quantify the path of the stream and search for additional members. We then quantify the stream’s morphology and estimate its luminosity.

4.1 Defining a native coordinate system

As a satellite orbits the Galaxy, its trajectory follows a path that is closely represented by the best fit great circle (Johnston et al. 1996; Ibata et al. 2001). For a relatively distant stream such as NGC 5466 that clearly spans several tens of degrees, a great circle fit in the heliocentric frame is a good approximation to the Galactocentric equivalent, and is highly convenient as a frame in which to quantify the stream’s properties. Positions on the celestial sphere are given in (ϕ_1, ϕ_2) which describe the longitude and latitude, respectively, of the great circle.

For the NGC 5466 reference frame, we determined the best fit pole of the great circle plane using stars from the gold sample. We used a least-squares minimization to minimize the scatter of stars in the ϕ_2 coordinate such that the origin of this system is centered on the cluster. The resulting plane is defined by its pole at $(\alpha_P, \delta_P) =$

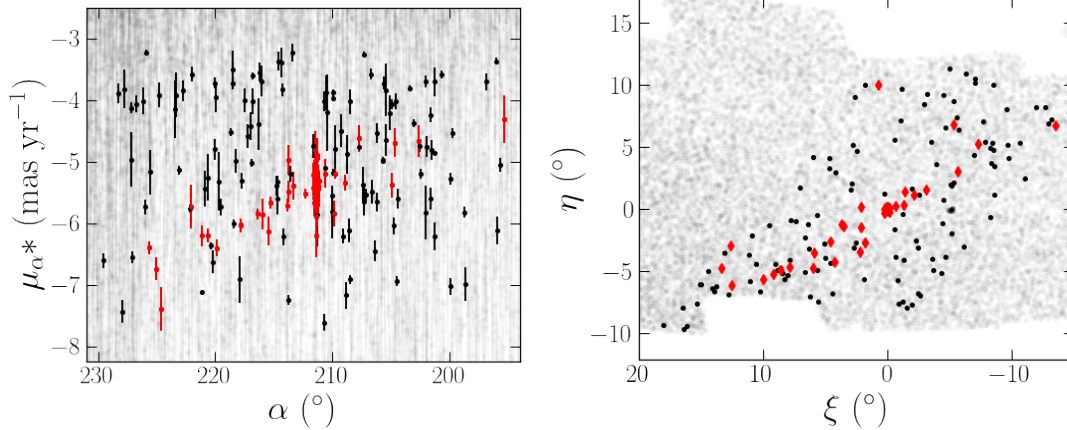


Figure 6. Left panel shows the proper motions (not corrected for Solar reflex motion) of RGB stars as a function of α , not corrected for Solar motion. The right panel is the tangent plane of the same data. For both plots, grey points are the full RGB sample, black are the filtered sample, and red represent stars surviving the sigma-clipping routine.

$(-16.86 \pm 0.83^\circ, 50.77 \pm 0.46^\circ)$. The transformation from equatorial to stream coordinates is given by:

$$\begin{bmatrix} \cos(\phi_1) \cos(\phi_2) \\ \sin(\phi_1) \cos(\phi_2) \\ \sin(\phi_2) \end{bmatrix} = R \times \begin{bmatrix} \cos(\alpha) \cos(\delta) \\ \sin(\alpha) \cos(\delta) \\ \sin(\delta) \end{bmatrix} \quad (2)$$

where the rotation matrix R is:

$$R = \begin{bmatrix} -0.7500 & -0.4572 & 0.4780 \\ -0.2664 & 0.8702 & 0.4144 \\ 0.6054 & -0.1835 & 0.7745 \end{bmatrix} \quad (3)$$

Note that the x-axis must be inverted for the leading arm to correspond with increasing ϕ_1 . The south-east to north-west extent of the stream in this frame begins at $(\alpha, \delta) \simeq (198^\circ, 36^\circ)$ and ends near $(\alpha, \delta) \simeq (229^\circ, 21^\circ)$.

Figure 7 shows the distribution of gold sample members (BHBs and RGBs as diamonds and circles, respectively) and giants within the cluster in this new frame of reference. The top panel shows the proper motion vectors for each star (scaled by 40%), corrected for Solar reflex motion (as in Section 3.1.3) and rotated into the great circle frame. In the bottom panel, the color scale represents the heliocentric distances for each star.

4.2 Searching for additional stream members

Prior to quantifying the properties of the stream, we first search for any additional members that may have been missed during our initial cuts. The kinematics of the gold sample stars are parameterized as a function of stream longitude. Specifically, we fit a polynomial to the proper motions in each direction as a function of ϕ_1 , and find a one-degree fit is favored over other models (as quantified via the Akaike Information Criterion, or AIC). Figure 8 shows the best fit polynomials to the proper motion data in each direction, where the dashed lines show the 3σ uncertainty in the slope of the fits.

Using these parameterizations, we search the RGB and BHB datasets within the range $\phi_1 = [-30^\circ, 30^\circ]$ for any stars that have proper motions consistent with those of the stream. For the RGBs, we also require that the stars have consistent metallicities to that of the cluster (i.e., $[\text{Fe}/\text{H}] = [-2.3, -1.7]$ dex). We consider a star a

candidate stream member if the 1σ range of its proper motion is consistent to that of the polynomial fits (to within three times the standard error of the fit, as shown by the dashed lines in Figure 8). An additional restriction required is that any putative members are within $|\phi_2| \leq 5^\circ$. As inspection of Figure 7 makes clear, this is a generous cut, and only removes stars that are clearly far away from the plane of the stream.

Finally, we look at the heliocentric distances of the remaining stars and compare them to the trend of R_{helio} vs ϕ_1 . We find two additional possible members using this method. These stars are appended to Table 2 and we show them in Figures 7 and 8 in red.

4.3 Quantifying the stream's properties

4.3.1 Length and width

The maximum difference in longitude between the putative stream members is $\sim 31^\circ$, including the new member stars identified in the preceding section. We adopt this value as the length of (the visible part of) the stream. However, the stream's length may very well continue in the trailing arm ($\phi_1 < -15^\circ$), where the trajectory approaches the limits of the CFIS footprint. This also corresponds to the approximate bounds of the SDSS detection made by Grillmair & Johnson (2006).

We estimate the stream's width by using the distribution of stars in ϕ_2 , beyond 1° from the cluster center. We find the width dispersion of this stream is $\sigma_w = (1.31 \pm 0.24)^\circ$, similar to the detected width found in Grillmair & Johnson (2006). In physical units, this is $w = 367 \pm 67$ pc wide at the distance of NGC 5466. We note in Section 6 there are a handful of RGBs which may be considered outliers (see also bottom left panel in Figure 10). After removing these stars, we obtain a similar width dispersion of $\sigma_w = (1.14 \pm 0.22)^\circ$, or equivalently, $w = 318 \pm 61$ pc wide.

The relative sparseness of stars in the leading arm ($\phi_1 > 0^\circ$) to that of the trailing arm should be noted. Although the lack of stars at $\phi_2 > 10^\circ$ could be caused by completeness effects, especially due to the large distances in the leading arm, in practice this is unlikely. The most distant RGB we find in the stream has a *Gaia* G -band magnitude of 19.6, nearly 1.5 magnitudes brighter than the *Gaia* magnitude limit. We address a possible reason for this discrepancy in

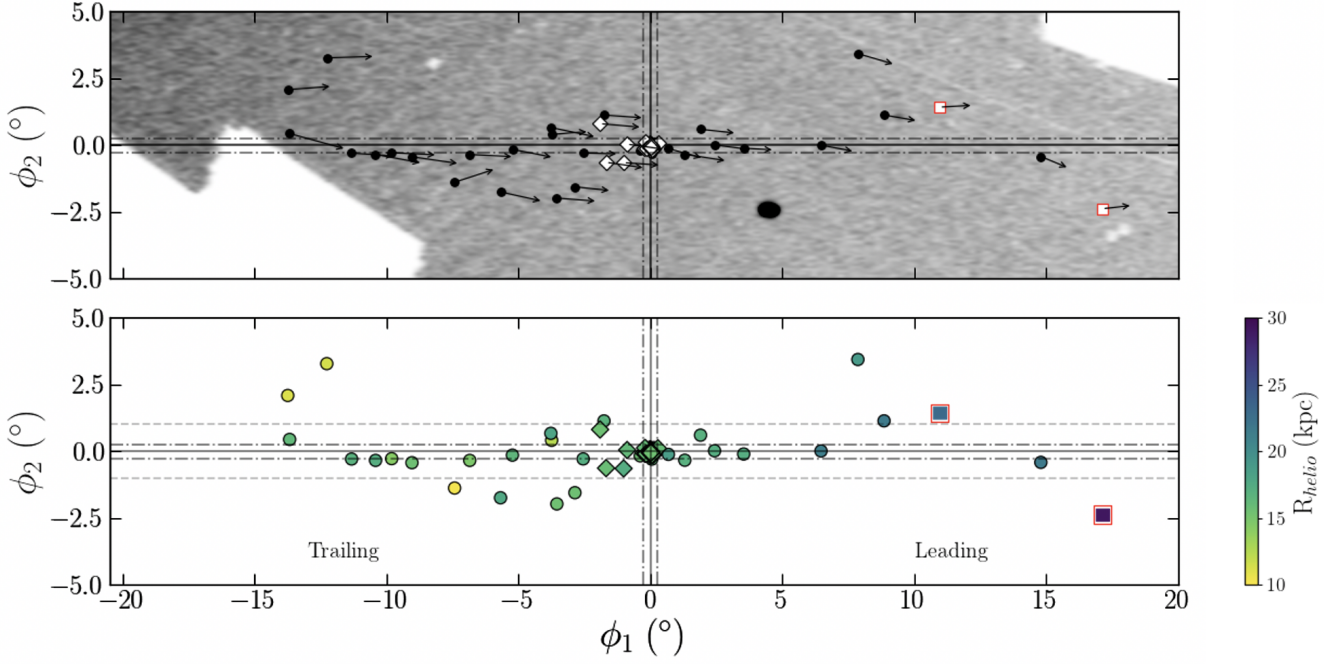


Figure 7. Gold sample RGBs (circles) and BHBs (diamonds) in the stream coordinate system. Vectors in the top panel are the proper motions corrected for Solar reflex motion, and rotated into the great circle frame. We show the limits of the CFIS footprint as the grey-filled region, where the dense circle at $(\phi_1, \phi_2) \sim (5^\circ, -2.5^\circ)$ is the nearby cluster, M 3. Colors of stars in the bottom panel correspond to their heliocentric distances. Most of the stars identified are within 1° of the ϕ_2 plane, shown as the dashed lines in the bottom panel. Dashed-dotted lines signify $\pm r_t$ (tidal radius). The two additional member stars identified in Section 4.2 are plotted in red.

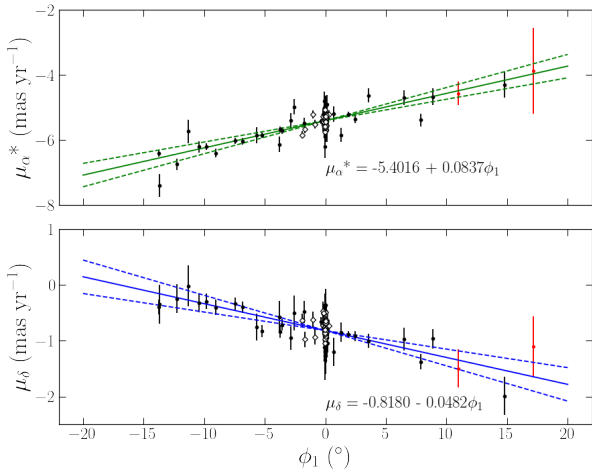


Figure 8. Proper motions, uncorrected for Solar reflex motion, as a function of ϕ_1 . Point styles are the same as in Figure 7 and additional members have been appended in red. The best fit trends are shown as solid lines. Dashed lines represent three times the standard error on the fitted slopes.

stream density, which could be due to the cluster’s past interactions with the Galaxy, in Section 6.

4.3.2 Luminosity

To determine a lower limit for the luminosity of the stream, we compare the number of giants identified within the tidal radius of NGC 5466 to those of the gold sample. We parameterize the

cluster’s density as a King profile and calculate the fraction of light in radial bins between $[0.77r_h, r_t]$ using parameters from Table 1. The lower limit of this range is set such that we avoid the central most regions of the cluster, where crowding effects in the CFIS data become significant. The fraction of light in this range is 29.5% of the luminosity of the entire cluster.

We estimate the number of giants (both RGBs and BHBs) between $[0.77r_h, r_t]$ to be 129 ± 11 . To estimate the total number of detectable giants, we extrapolate this profile and find 437 ± 21 giants within the tidal radius. We compare this to the 36 giants we identify as stream members in this work, yielding a ratio of stars in the stream to those in the main body is 0.082 ± 0.004 .

NGC 5466’s absolute visual magnitude is $M_V = -6.98$ mag, which equates to a total luminosity of $\sim 4.9 \times 10^4 L_{\odot}$. This implies that the luminosity of the detected part of the stream is $[4.0 \pm 0.2] \times 10^3 L_{\odot}$. Adopting a stellar mass-to-light ratio of ~ 1 (Pryor et al. 1991) means the stellar mass in the stream is roughly $4.0 \times 10^3 M_{\odot}$.

These estimations have a few caveats and should certainly only be considered as a lower limit. Most importantly, we only estimate the luminosity of the part of the stream that we have been able to detect. Lower surface brightness parts of the stream are not accounted for in this calculation, and of course we have no information on the stream beyond the CFIS footprint. Additionally, the stream detection is extremely sparse. For the 36 giants we identify in the stream, and given the length and width we estimated, this corresponds to a density of 0.55 ± 0.07 bright giants deg $^{-2}$.

Table 2. List of “Gold Sample” giants. IDs with an asterisk (*) are the possible contaminants identified in Figure 10. The tentative final members added in Section 4.2 are marked with double (**).

No.	Population	α ($^{\circ}$)	δ ($^{\circ}$)	R_{helio} (kpc)	μ_{α}^* (mas yr $^{-1}$)	μ_{δ} (mas yr $^{-1}$)	ϕ_1 ($^{\circ}$)	ϕ_2 ($^{\circ}$)	μ_{ϕ_1} (mas yr $^{-1}$)	μ_{ϕ_2} (mas yr $^{-1}$)
1	BHB	212.0302	27.5003	17.2967 \pm 1.7297	-5.2112 \pm 0.1305	-0.6172 \pm 0.1437	-1.0169	-0.6473	3.5773	-0.2422
2	BHB	211.1383	28.7820	15.9393 \pm 1.5939	-5.2123 \pm 0.1166	-0.7325 \pm 0.1044	0.2826	0.1094	3.4694	-0.0848
3	BHB	212.2727	28.1715	16.2251 \pm 1.6225	-5.5180 \pm 0.1349	-0.9305 \pm 0.1404	-0.8848	0.0448	3.6424	-0.4972
4	BHB	212.6950	27.1924	15.8071 \pm 1.5807	-5.6548 \pm 0.1249	-0.9769 \pm 0.1363	-1.6828	-0.6347	3.7182	-0.5320
5	BHB	213.7126	28.3461	15.5797 \pm 1.5580	-5.8405 \pm 0.1152	-0.6391 \pm 0.1208	-1.9106	0.8110	4.0074	-0.3401
6	BHB	211.6359	28.5638	16.0564 \pm 1.6056	-5.4169 \pm 0.1140	-0.4610 \pm 0.1307	-0.2053	0.1230	3.7772	0.0175
7	RGB	195.3068	34.2154	21.6520 \pm 1.3741	-4.3092 \pm 0.3881	-1.9872 \pm 0.3450	14.8034	-0.4181	2.6937	-1.1015
8	RGB	202.6499	33.4567	21.6475 \pm 1.8703	-4.6716 \pm 0.2569	-0.9615 \pm 0.1753	8.8576	1.1352	3.2370	-0.5511
9	RGB	204.6825	31.4458	21.3098 \pm 1.6581	-4.6976 \pm 0.2340	-0.9712 \pm 0.2021	6.4674	0.0071	3.2133	-0.5985
10	RGB	204.8897	35.1409	18.9778 \pm 2.0912	-5.3810 \pm 0.1986	-1.3792 \pm 0.1389	7.8654	3.4324	3.5611	-1.0257
11	RGB	207.7039	30.0776	17.2575 \pm 1.2324	-4.6257 \pm 0.2220	-1.0034 \pm 0.1258	3.5350	-0.1058	2.9362	-0.1681
12	RGB	208.9051	29.6896	17.2590 \pm 1.2863	-5.3480 \pm 0.1310	-0.9136 \pm 0.0914	2.4302	0.0147	3.6020	-0.4556
13	RGB	209.8709	28.8610	16.9963 \pm 0.8251	-5.8456 \pm 0.2130	-0.8476 \pm 0.1748	1.3021	-0.3374	4.0484	-0.6151
14	RGB	209.7578	29.9678	17.0305 \pm 0.8117	-5.2011 \pm 0.0765	-0.8851 \pm 0.0542	1.8989	0.5999	3.4566	-0.3642
15	RGB	211.1529	28.3138	16.4268 \pm 0.4823	-5.3972 \pm 0.0669	-0.9246 \pm 0.0661	0.0512	-0.2978	3.5681	-0.4263
16	RGB	210.6149	28.7657	18.6889 \pm 1.0345	-5.1982 \pm 0.2352	-1.2038 \pm 0.2508	0.6804	-0.1198	3.3623	-0.9172
17	RGB	211.6564	28.2156	15.5932 \pm 0.7845	-5.4239 \pm 0.0779	-0.6604 \pm 0.0823	-0.3861	-0.1750	3.6677	-0.0695
18	RGB	213.3529	25.8162	15.6223 \pm 0.9959	-5.3910 \pm 0.2285	-0.9500 \pm 0.2119	-2.8641	-1.5543	3.4879	-0.3571
19	RGB	213.7877	25.1158	15.5186 \pm 0.5563	-5.7101 \pm 0.1064	-0.7134 \pm 0.0967	-3.5489	-1.9741	3.8738	-0.2963
20	RGB	213.7368	27.0737	17.2229 \pm 0.8812	-4.9750 \pm 0.2347	-0.5004 \pm 0.3135	-2.5511	-0.2887	3.4015	-0.0761
21	RGB	213.7444	28.6991	16.8205 \pm 1.1477	-5.4889 \pm 0.1831	-0.4822 \pm 0.1947	-1.7624	1.1325	3.8318	-0.2637
22	RGB	215.2901	27.0877	12.4913 \pm 0.4596	-5.6743 \pm 0.0975	-0.8364 \pm 0.1119	-3.7466	0.4070	3.5615	0.2789
23	RGB	215.4653	27.2993	18.0070 \pm 1.0454	-6.1283 \pm 0.2307	-0.5721 \pm 0.2842	-3.7757	0.6681	4.3691	-0.9047
24	RGB	215.9519	24.2550	17.7626 \pm 1.8410	-5.8570 \pm 0.2503	-0.7543 \pm 0.2383	-5.6841	-1.7440	4.0432	-0.8798
25	RGB	216.4128	25.8587	16.4943 \pm 0.7597	-5.8503 \pm 0.0857	-0.8306 \pm 0.1060	-5.2335	-0.1493	3.9321	-0.7682
26*	RGB	217.7949	23.6799	10.3904 \pm 0.4976	-6.0207 \pm 0.0979	-0.3381 \pm 0.1120	-7.4265	-1.3794	3.9355	1.2545
27	RGB	217.8405	24.8631	14.7913 \pm 0.9061	-6.0378 \pm 0.1080	-0.3962 \pm 0.1034	-6.8513	-0.3446	4.2221	-0.2042
28	RGB	219.8409	23.6443	15.5834 \pm 0.8387	-6.4060 \pm 0.1342	-0.4024 \pm 0.1373	-9.0432	-0.4306	4.5507	-0.6402
29	RGB	221.1630	22.9827	17.2438 \pm 0.7690	-6.2060 \pm 0.1721	-0.3184 \pm 0.1686	-10.4232	-0.3438	4.4759	-0.8088
30	RGB	220.6388	23.3639	14.3005 \pm 0.6498	-6.2007 \pm 0.1058	-0.2952 \pm 0.1365	-9.8121	-0.2797	4.3653	-0.1946
31	RGB	222.0228	22.5356	16.9056 \pm 1.3742	-5.7303 \pm 0.3589	-0.0170 \pm 0.3709	-11.3320	-0.2929	4.2191	-0.2725
32	RGB	224.5786	21.8593	16.3049 \pm 1.0889	-7.3919 \pm 0.3478	-0.3471 \pm 0.3517	-13.6814	0.4400	5.3777	-1.4567
33*	RGB	225.0265	24.9984	11.4767 \pm 0.8607	-6.7452 \pm 0.1837	-0.2462 \pm 0.2571	-12.2730	3.2758	4.6083	0.1346
34*	RGB	225.6367	23.1840	11.2105 \pm 0.4497	-6.4005 \pm 0.1028	-0.3936 \pm 0.1299	-13.7523	2.0848	4.2402	0.3159
35**	RGB	191.8986	33.1122	29.1899 \pm 3.0057	-3.8701 \pm 1.3128	-1.1017 \pm 0.5421	17.1370	-2.3727	2.8652	0.3140
36**	RGB	200.4530	34.5566	23.0920 \pm 1.7470	-4.5673 \pm 0.3618	-1.4991 \pm 0.3415	10.9650	1.4306	3.1950	0.1719

5 MODELLING THE DYNAMICS OF NGC 5466

Given the difficulty of earlier work in matching the path of the stream as defined by Grillmair & Johnson (2006), we now examine some simple dynamical models to aid in our understanding of NGC 5466’s orbital history. We consider both a point-mass orbit and a particle-spray model (see Fardal et al. 2015 for details) which we implement using the PYTHON-wrapped package known as GALA (Price-Whelan 2017).

We use a right-handed Galactocentric coordinate system such that the Sun is located at $(X, Y, Z) = (-8.122, 0.0, 0.025)$ kpc, with LSR velocities of $[U, V, W]_{\odot} = [11.1, 12.24, 7.25]$ km s $^{-1}$ (as in Section 3.1.3). The Milky Way potential is fixed using a three-component model, consisting of a Miyamoto & Nagai (1975) disk, a Hernquist (1990) bulge, and spherical NFW dark matter halo (Navarro et al. 1996):

$$\Phi_{bulge}(R) = \frac{-GM_b}{R+a} \quad (4)$$

$$\Phi_{disk}(R_{cyl}, z) = \frac{-GM_d}{\sqrt{R_{cyl}^2 + (b + \sqrt{z^2 + c^2})^2}} \quad (5)$$

$$\Phi_{halo}(R) = \frac{-4\pi G \rho_s r_s^3}{R} \ln\left(1 + \frac{R}{r_s}\right) \quad (6)$$

where R is the Galactocentric radius, R_{cyl} is the cylindrical radius, and z is the vertical height above the disk.

Our chosen values for masses, scale radii, and other parameters are summarized in Table 3. For the disk, the mass (M_d), scale height (b), and scale length (c) are the values used in the MWPotential2014 from Bovy (2015). For the halo, we adopt recent estimates for the Milky Way virial mass and radius (M_{vir} and R_{vir} , respectively) from Cautun et al. (2020). Assuming a dark matter concentration of 12 (a typical value observed in simulated Milky Way analogues; see Boylan-Kolchin et al. 2010) and using the relation $R_{vir} = c_h R_s$, we adopt a scale height for the dark matter halo of 17.25 kpc. These parameters produce a circular velocity at the Sun similar to the estimate from Eilers et al. (2019) ($v_{circ}(R_{\odot}) = 229$ km s $^{-1}$).

Table 3. Galactic potential parameters.

Component	Parameter	Value
Bulge	M_b	$5 \times 10^9 M_\odot$
	a	1 kpc
Disk	M_d	$5.56 \times 10^{10} M_\odot$
	b	3.5 kpc
	c	280 pc
Halo	M_{vir}	$8.2 \times 10^{11} M_\odot$
	R_{vir}	207 kpc
	c_h	12
	r_s	17.25 kpc

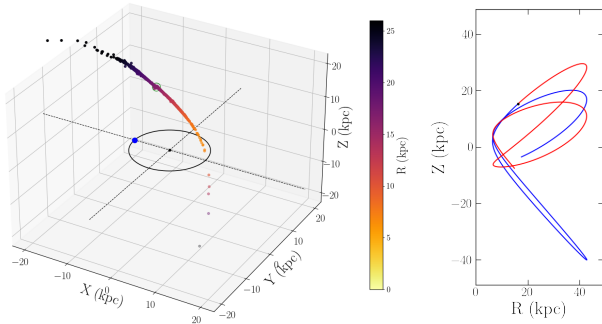


Figure 9. Orbit integrations of NGC 5466 in the Galactic frame. The left plot shows a 3D representation of the sprayed particles, where the scaled colors correspond to Galactocentric radius (R). We also show the Solar circle where the Sun is located at the blue point. In the right panel, the blue and red trajectories are the backwards and forwards point-mass orbit integrations of NGC 5466.

For our particle-spraying simulations, we account for the internal gravity of the satellite, represented as a spherical [Plummer \(1911\)](#) profile:

$$\Phi_p(r) = \frac{-GM_{sat}}{\sqrt{r^2 + d^2}} \quad (7)$$

We used the present-day stellar mass of NGC 5466 and a scale length (d) of 6.7 pc derived from the core radius of the cluster (see [Table 1](#)).

The point-mass orbit of NGC 5466 was integrated forwards and backwards in time by 1 Gyr to examine the trajectory of the cluster in our chosen Galactic potential. This serves as a rough estimate to the most likely path of the stream.

For the particle-spray method, we initiated the cluster 2 Gyrs ago and ran the model forward in time, releasing one particle at each Lagrange point per timestep (for a total of 1,000 timesteps every 100 Myrs). Mass loss is not explicitly tracked in this method, therefore saving on computation time; however, each ejected particle is provided orbit information based on the current position and velocity of the progenitor and integrated forward with the cluster, allowing the stream’s evolution to be mapped in phase-space. We examine the qualitative resemblances between the observational data and dynamical model in the following section.

6 DISCUSSION

We show the point-mass trajectory of the cluster in [Figure 9](#), where the backwards and forwards orbit integrations are represented as blue and red lines, respectively. From this estimation, we find that the pericenter is approximately 6.42 kpc, apocenter is 42.99 kpc, and the eccentricity of NGC 5466’s orbit is 0.74. These values agree closely with those estimated in [Baumgardt et al. \(2019\)](#).

We note two significant points from the (R , z) panel on the right in [Figure 9](#): firstly, the cluster’s most recent pericentric passage occurred ~ 50 Myrs ago, and secondly, NGC 5466 recently crossed the Galactic disk. Both interactions (especially at nearly the same time) suggest significant and recent mass loss. Previous simulations modeling the cluster’s detailed disruption have obtained similar conclusions, claiming that NGC 5466 has suffered disk-shocking ([Odenkirchen & Grebel 2004](#); [Fellhauer et al. 2007](#)). In particular, [Fellhauer et al. \(2007\)](#) used SUPERBOX particle-mesh simulations fit to the stream’s surface density and width based on the matched filter path given by the [Grillmair & Johnson \(2006\)](#) detection, and present-day cluster measurements given by HIPPARCOS and [Harris \(1996\)](#). Their work suggested that the tidal tails of NGC 5466 could be as lengthy as 100° on the sky – for comparison, this is nearly the same order as the length of the Sagittarius stream ([Ibata et al. 2002](#); [Majewski et al. 2003](#)). Though it would be worthwhile to calculate an updated, post-*Gaia* estimate for the cluster’s disruption, we consider it beyond the present scope of this work. We leave it to future efforts to utilize *Gaia* astrometry with more detailed simulations matched to the gold sample.

Though the purpose of the particle-spray model was to compare the kinematic trends of star particles to our gold sample (and not to model the disruption of NGC 5466 over time), we find good agreement between observations and our simple model. [Figure 10](#) shows the proper motions and heliocentric distances as functions of ϕ_1 , where the particles are represented as black points and the gold sample members are shown as grey error bars. We find that the global behavior of the proper motions is well-replicated by the model as a function of longitude. However, our simplistic model appears to systematically underestimate the distances in the leading arm (although there are not as many identified points at these larger distances). It is quite possible that this divergence may be a result of the spherical dark matter halo shape we implemented; alternatively, it could perhaps be due to an interaction with another satellite. Our preliminary analysis suggests NGC 5466 may have passed close to the LMC in its recent trajectory; however, this requires more investigation with a time-dependent potential.

There are three gold sample members in [Figure 10](#) whose proper motions are consistent with the rest of the data and the model, but whose distances do not follow the global trends. We consider these three points, highlighted with red circles, as outliers/contamination, and they are noted in [Table 2](#) with an asterisk. We note that these additional members do not greatly affect estimates for the stream width, mass, or length.

Lastly, we cross-matched the gold sample to spectra available from LAMOST (Large sky Area Multi-Object Fiber Spectroscopic Telescope; [Luo et al. 2015](#)) and obtained radial velocities for six gold sample members. We show the comparison between LAMOST DR6 radial velocities to GALA particles, which indeed appear consistent for all except one star that has already been labeled a contaminant based on its heliocentric distance. Summarized observational data for these stars are located in [Table 4](#).

Given that we find broad agreement between data and model, we also compare to previous simulations of NGC 5466. Two works

Table 4. Six cross-matched stars observed in LAMOST DR6. Numbers in first column associate these stars to the data in Table 2. The star with (*) is highlighted as a contaminant based on its discrepant distance.

No.	LAMOST ID	α ($^{\circ}$)	δ ($^{\circ}$)	v_r (km s^{-1})
1	J140807.25+273001.2	212.0302	27.5003	92.6 ± 5.4
11	J135048.93+300439.3	207.7039	30.0776	98.8 ± 15.9
12	J135537.21+294122.9	208.9051	29.6896	105.9 ± 16.7
17	J140637.54+281256.3	211.6564	28.2156	111.4 ± 9.0
25	J141458.68+284156.5	216.4128	25.8587	84.6 ± 7.3
34*	J150232.78+231102.6	225.6367	23.1840	75.8 ± 4.2

in particular found opposing conclusions, though both relied on the observed stream path given by the matched filter of Grillmair & Johnson (2006). Critically, Fellhauer et al. (2007) found that it was not possible to reproduce the stream with the current proper motion estimate for the globular cluster. At the time of their study, the proper motions were derived from HIPPARCOS, which yielded $(\mu_{\alpha^*}, \mu_{\delta}) = (-4.65 \pm 0.82, +0.8 \pm 0.82) \text{ mas yr}^{-1}$. The authors opted for a lower value of $\mu_{\delta} = 0.4 \text{ mas yr}^{-1}$ (within 1σ of the measurement) to best fit the tails. Compared to the more recent *Gaia*-based estimate derived by Baumgardt et al. (2019), $\mu_{\delta} = -0.79 \pm 0.01$, their correction is closer to the more recent estimate. Overall, Fellhauer et al. (2007) predicted a trend in heliocentric distance that is generally consistent with our new findings.

Lux et al. (2012) developed a second dynamical model of NGC 5466 using the orbit-fitting method to constrain the Galactic potential. Interestingly, they reproduced the path of the stream up to $\alpha = 192^{\circ}$ (we note that it is at $\sim 195^{\circ}$ where we no longer detect any stream members) using oblate and triaxial halo shapes and claimed that spherical and prolate dark matter halos could be rejected at high confidence. However, the gradient in heliocentric distances predicted by Lux et al. (2012) demonstrates the opposite trend of both Fellhauer et al. (2007) and our new observations, such that stars in their model are at close distances of $\sim 10 \text{ kpc}$ in the leading arm ($\phi_1 > 15^{\circ}$; see Figure 3 in Lux et al. 2012). We note that, at the time of these studies, there was no direct information on the distance gradient or proper motions of stars in the stream for comparison.

It is worthwhile to examine the position of the stream as detected in CFIS to the matched filter detection of Grillmair & Johnson (2006), which we show in Figure 11. Grillmair & Johnson (2006) proposed that the dark diagonal strip from bottom left to top right corners of the plot is a stream from NGC 5466. We plot our great circle plane fit to the gold sample stars as a red line for comparison, and additionally highlight GALA star particles in blue. Close to the cluster, our findings broadly agree with Grillmair & Johnson (2006). However, at $\alpha \lesssim 200^{\circ}$, the trajectories of our great circle and model deviate from the claimed matched filter path, and indeed, we are unable to detect many stream members past this position. Given our analysis is based on deeper photometry (CFIS and PS1 3π , compared to SDSS), we consider it unlikely that the feature in the matched filter at these coordinates is a real signal. This would also serve to explain previous difficulties in matching models to these observations.

In this work, we kinematically detect the tidal tails of NGC 5466 despite the fact that the stream is a) extremely diffuse and b) very distant, such that *Gaia* DR2 parallaxes are of limited use. We attribute our success to the tracer populations which have been robustly identified with CFIS, such that we obtain excellent distance estimates for stars at large Galactocentric radius. Paired

with the exquisite proper motions in *Gaia* DR2, we are able to compile a detailed dataset of stars to explore the kinematic trends of this interesting stream. Though there have been many data-mining efforts implemented to probe *Gaia* DR2 for substructures (e.g., Mateu et al. 2018; Ibata et al. 2019; Necib et al. 2020; Borsato et al. 2020), our study is the only one to observe member stars of the NGC 5466 stellar stream within this dataset. Our work predated the arrival of *Gaia* eDR3, however, a recent study by Ibata et al. (2020) also identified some stars in the NGC 5466 stream using the STREAMFINDER algorithm (Malhan & Ibata 2018) applied to the newest *Gaia* release. In comparison, their detection identified mostly stars in the trailing arm and over a smaller angle on the sky than presented here.

7 SUMMARY

In this work, we explored substructure in the outer stellar halo using multiple tracer populations with CFIS. We first examined the spatial distribution of CFIS BHBs with OPTICS and identified several known satellites within the dataset, all of which showed some evidence of spatially extended stellar populations. Among these was the globular cluster NGC 5466, which is a distant cluster that had previously been argued to possess a long stellar stream, although no individual stellar members of the stream had been identified.

Given its potential use to help probe the dynamics of the outer halo, and given that previous dynamical studies had difficulties reproducing the reported properties of the stream, we chose to further explore this system. We confirmed association of several of the extra-tidal BHBs using cross-matched *Gaia* DR2 proper motions. By mining the expansive CFIS RGB dataset for stars whose kinematics and metallicities broadly represented that of the cluster, we found an extended stream from NGC 5466 that is both spatially and kinematically coherent.

Having identified stream members, we determined the stream's natural frame of reference and quantified its overall structure, dynamics, and stellar mass. We compared the observed behavior in proper motions and distances to simple dynamical models involving both a point mass and a GALA particle-spray model. We found that even these simple models are able to reproduce the global behavior of the stream's proper motion, and provide a good match to the observed distance gradient. Our work is the first to identify member stars of NGC 5466 both spatially and dynamically (predating *Gaia* eDR3), and we identify interesting systematic difference between observations and the models in the leading arm of the stream.

We anticipate these results will motivate future modeling and observing campaigns (e.g., radial velocities), which could provide some interesting insights into the global shape of the Milky Way halo at these large distances. Our GALA model implements a spherical NFW halo and successfully reproduces, to first order at least, the major trends we observe in proper motions and distances. Unlike the previous claim by Lux et al. (2012) based on earlier observations (which we show did not correctly trace the stream's path), it appears that the NGC 5466 stream cannot yet rule out a spherical halo shape. While NGC 5466 is only one stream out of a multitude of such structures, we expect it to be a very useful laboratory for those seeking to better measure the mass and shape of the Milky Way's gravitational potential. The fact that NGC 5466 is so distant, exhibits a strong distance gradient, has an identified progenitor, and is believed to have recently had an interaction with the Galaxy's disk, makes it a unique test-case for dynamical modelling of the Milky Way.

In the context of observational constraints on NGC 5466, we

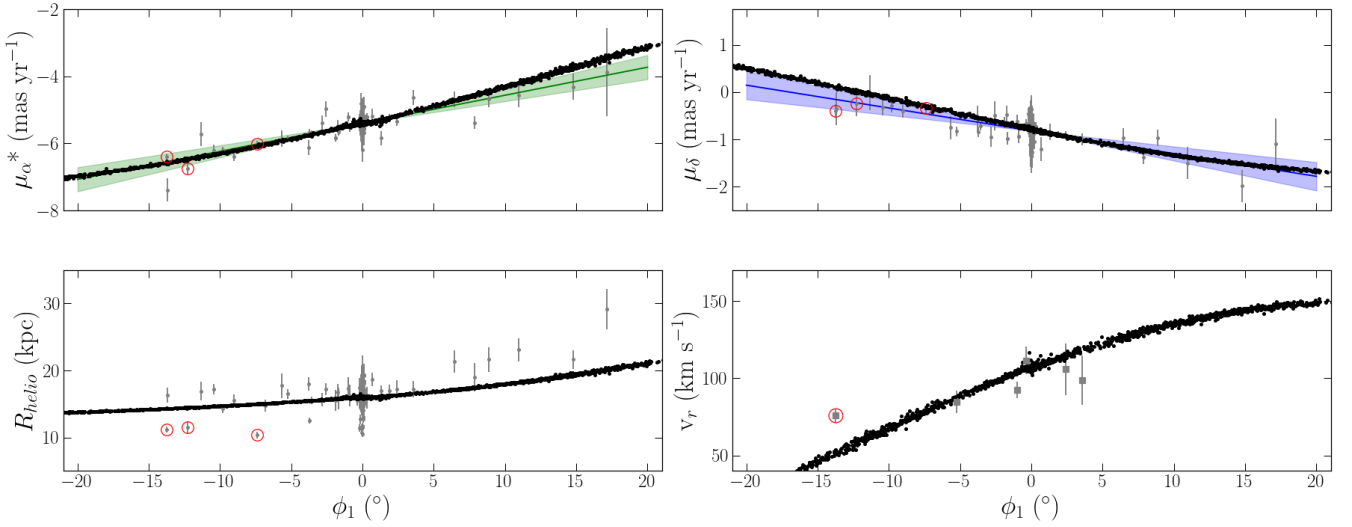


Figure 10. Comparison of kinematics against ϕ_1 in the gold sample stars (grey error bars) and sprayed particles from the dynamical model (black points). The top panels show uncorrected proper motions in α and δ , where the highlighted ranges show the upper and lower bounds of the fitted lines (same as in Figure 8). We show the heliocentric distances in the bottom left panel. Based on their discrepant distances, three gold sample members are highlighted in each panel with red circles. The final panel in the bottom right show the line-of-sight velocities for six stars present in LAMOST. Note that one particular outlier at $(\phi_1, R_{\text{helio}}) = (-13.7^\circ, 11.2 \text{ kpc})$ corresponds to the red circle in the final panel, which further confirms this star is an outlier based on its inconsistent radial velocity.

anticipate that the dynamical properties of the stream quantified in Section 4.2 will help in identifying additional member stars. This is a particular priority for the trailing arm, which could well extend beyond the SDSS and CFIS footprints. The other obvious observational constraint currently lacking from our analysis are the radial velocities for member stars. In this era of *Gaia*, it is increasingly the case that tangential velocities are more readily available than radial velocities, the exact opposite of what it has been for many decades. However, obtaining the stream’s full 6-D kinematics will allow us to explore the phase-space distribution in detail – including deriving energies and angular momenta for our member stars. With spectra of sufficiently high resolution, we can also better explore the chemical abundances of our stream sample. Already, this type of analysis on the main body has shown trends in α -elements similarly observed in dwarf galaxies (Venn et al. 2004; Lamb et al. 2015), and follow-up spectra of $[\alpha/\text{Fe}]$ abundances along the NGC 5466 stream should soon be possible with WEAVE (Dalton et al. 2012).

It is notable that this stream was identified in *Gaia* DR2 when combined with photometric parallaxes from CFIS, that currently do not cover the full intended footprint of this survey. Using the all-sky power of *Gaia*, and the wide field u -band perspective of CFIS for $10,000 \text{ deg}^2$ in the north, soon to be followed by the Legacy Survey of Space and Time (LSST at the Vera C. Rubin Observatory) in the south, our exploration of the outer Galaxy is only just beginning.

ACKNOWLEDGEMENTS

GT acknowledge support from the Agencia Estatal de Investigación (AEI) of the Ministerio de Ciencia e Innovación (MCINN) under grant with reference (FJC2018-037323-I). RI acknowledges funding from the European Research Council (ERC) under the European Unions Horizon 2020 research and innovation programme (grant agreement No. 834148). NFM and RI gratefully acknowledge sup-

port from the French National Research Agency (ANR) funded project “Pristine” (ANR-18-CE31-0017)

The work detailed above was conducted at the University of Victoria in Victoria, British Columbia, as well as in the Township of Esquimalt in Greater Victoria. We acknowledge with respect the Lekwungen peoples on whose unceded traditional territory the university stands, and the Songhees, Esquimalt and WSÁNEĆ peoples whose historical relationships with the land continue to this day.

CFIS is conducted at the Canada-France-Hawaii Telescope on Maunakea in Hawaii. We also recognize and acknowledge with respect the cultural importance of the summit of Maunakea to a broad cross section of the Native Hawaiian community.

This work is based on data obtained as part of the Canada-France Imaging Survey (CFIS), a CFHT large program of the National Research Council of Canada and the French Centre National de la Recherche Scientifique. Based on observations obtained with MegaPrime/MegaCam, a joint project of CFHT and CEA Saclay, at the Canada-France-Hawaii Telescope (CFHT) which is operated by the National Research Council (NRC) of Canada, the Institut National des Science de l’Univers (INSU) of the Centre National de la Recherche Scientifique (CNRS) of France, and the University of Hawaii.

The Pan-STARRS1 Surveys (PS1) and the PS1 public science archive have been made possible through contributions by the Institute for Astronomy, the University of Hawaii, the Pan-STARRS Project Office, the MaxPlanck Society and its participating institutes, the Max Planck Institute for Astronomy, Heidelberg and the Max Planck Institute for Extraterrestrial Physics, Garching, The Johns Hopkins University, Durham University, the University of Edinburgh, the Queen’s University Belfast, the Harvard-Smithsonian Center for Astrophysics, the Las Cumbres Observatory Global Telescope Network Incorporated, the National Central University of Taiwan, the Space Telescope Science Institute, the National Aeronautics and Space Administration under Grant No. NNX08AR22G issued through the Planetary Science Division of the NASA Science

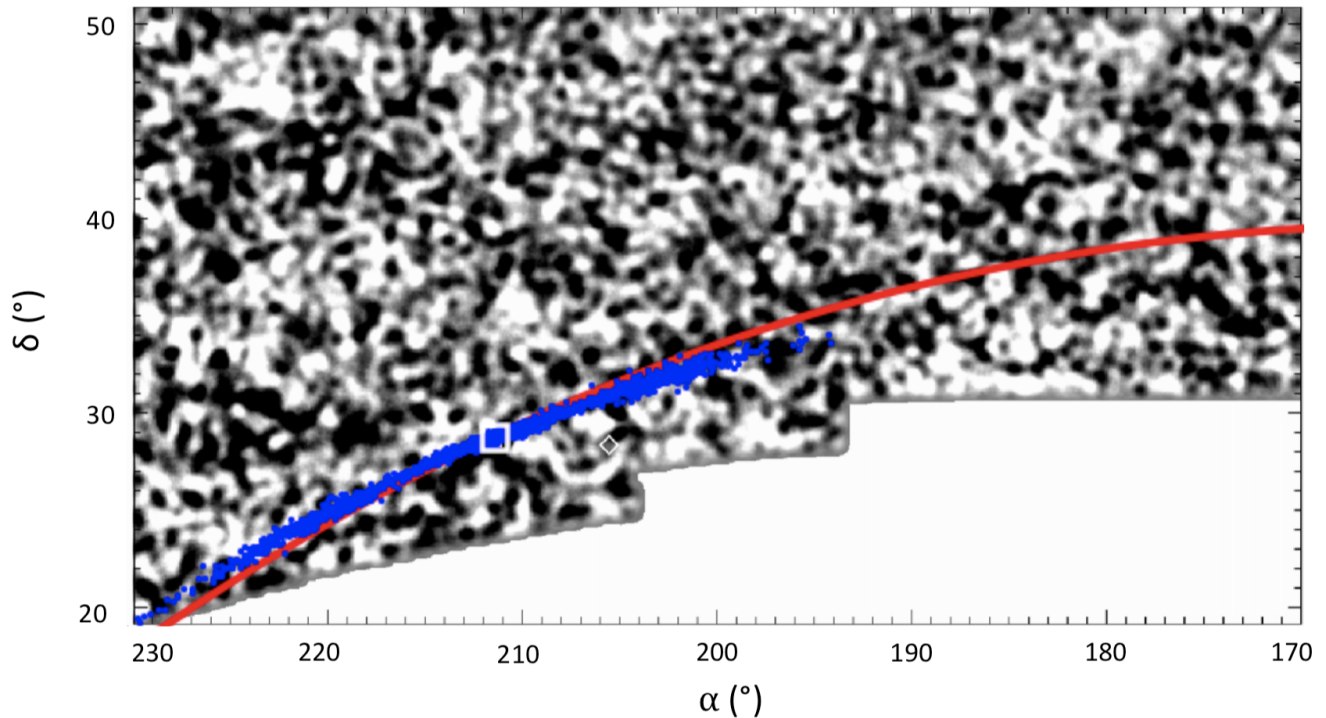


Figure 11. A direct comparison between the 45° detection from Grillmair & Johnson (2006) to this work. The path of the extended tails is claimed to begin at $(\alpha, \delta) = (230^\circ, 20^\circ)$ and end near $(180^\circ, 42^\circ)$. We overlay the great circle longitude (ϕ_1 ; red line) and GALA star particles (blue) on the matched filter map. Both diverge at approximately $\alpha = 200^\circ$ compared to the original detection. NGC 5466 is represented with a white square and the nearby globular cluster M 3 (NGC 5272) as the diamond.

Mission Directorate, the National Science Foundation Grant No. AST-1238877, the University of Maryland, Eotvos Lorand University (ELTE), the Los Alamos National Laboratory, and the Gordon and Betty Moore Foundation.

This work has made use of data from the European Space Agency (ESA) mission *Gaia* (<https://www.cosmos.esa.int/gaia>), processed by the *Gaia* Data Processing and Analysis Consortium (DPAC, <https://www.cosmos.esa.int/web/gaia/dpac/consortium>). Funding for the DPAC has been provided by national institutions, in particular the institutions participating in the *Gaia* Multilateral Agreement.

DATA AVAILABILITY

The gold sample stars from the NGC 5466 stream are made available in the article and in its online supplementary material. A subset of the raw data underlying this article are publicly available via the Canadian Astronomical Data Center at <http://www.cadc-ccda.hia-ihp.nrc-cnrc.gc.ca/en/megapipe/>. The remaining raw data and all processed data are available to members of the Canadian and French communities via reasonable requests to the principal investigators of the Canada-France Imaging Survey, Alan McConnachie and Jean-Charles Cuillandre. All data will be publicly available to the international community at the end of the proprietary period, scheduled for 2023.

REFERENCES

- Ankerst M., Breunig M. M., Kriegl H., Sander J., 1999. ACM Press, pp 49–60
- Baumgardt H., Hilker M., Sollima A., Bellini A., 2019, *MNRAS*, **482**, 5138
- Bellazzini M., Ibata R., Malhan K., Martin N., Famaey B., Thomas G., 2020, *A&A*, **636**, A107
- Belokurov V., Evans N. W., Irwin M. J., Hewett P. C., Wilkinson M. I., 2006, *ApJ*, **637**, L29
- Bianchini P., Ibata R., Famaey B., 2019, *ApJ*, **887**, L12
- Bonaca A., Hogg D. W., 2018, *ApJ*, **867**, 101
- Borsato N. W., Martell S. L., Simpson J. D., 2020, *MNRAS*, **492**, 1370
- Boulade O., et al., 2003, in Iye M., Moorwood A. F. M., eds, Society of Photo-Optical Instrumentation Engineers (SPIE) Conference Series Vol. 4841, Instrument Design and Performance for Optical/Infrared Ground-based Telescopes. pp 72–81, doi:10.1117/12.459890
- Bovy J., 2015, *ApJS*, **216**, 29
- Boylan-Kolchin M., Springel V., White S. D. M., Jenkins A., 2010, *MNRAS*, **406**, 896
- Carlin J. L., Sand D. J., 2018, *ApJ*, **865**, 7
- Carlin J. L., Grillmair C. J., Muñoz R. R., Nidever D. L., Majewski S. R., 2009, *ApJ*, **702**, L9
- Cautun M., et al., 2020, *MNRAS*, **494**, 4291
- Chambers K. C., et al., 2016, arXiv e-prints, p. arXiv:1612.05560
- Dalton G., et al., 2012, in McLean I. S., Ramsay S. K., Takami H., eds, Society of Photo-Optical Instrumentation Engineers (SPIE) Conference Series Vol. 8446, Ground-based and Airborne Instrumentation for Astronomy IV. p. 84460P, doi:10.1117/12.925950
- Deason A. J., Belokurov V., Evans N. W., 2011, *MNRAS*, **416**, 2903
- Eilers A.-C., Hogg D. W., Rix H.-W., Ness M. K., 2019, *ApJ*, **871**, 120
- Ester M., Kriegl H.-P., Sander J., Xu X., 1996. AAAI Press, pp 226–231
- Fardal M. A., Huang S., Weinberg M. D., 2015, *MNRAS*, **452**, 301

- Farrow D. J., et al., 2014, *MNRAS*, **437**, 748
- Fellhauer M., Evans N. W., Belokurov V., Wilkinson M. I., Gilmore G., 2007, *MNRAS*, **380**, 749
- Gaia Collaboration et al., 2016, *A&A*, **595**, A1
- Gaia Collaboration et al., 2018, *A&A*, **616**, A1
- Gaia Collaboration Brown A. G. A., Vallenari A., Prusti T., de Bruijne J. H. J., Babusiaux C., Biermann M., 2020, arXiv e-prints, p. [arXiv:2012.01533](https://arxiv.org/abs/2012.01533)
- Gravity Collaboration et al., 2019, *A&A*, **625**, L10
- Grillmair C. J., 2009, *ApJ*, **693**, 1118
- Grillmair C. J., Carlin J. L., 2016, Stellar Streams and Clouds in the Galactic Halo. p. 87, [doi:10.1007/978-3-319-19336-6_4](https://doi.org/10.1007/978-3-319-19336-6_4)
- Grillmair C. J., Johnson R., 2006, *ApJ*, **639**, L17
- Harris W. E., 1996, *AJ*, **112**, 1487
- Helmi A., Veljanoski J., Breddels M. A., Tian H., Sales L. V., 2017, *A&A*, **598**, A58
- Helmi A., Babusiaux C., Koppelman H. H., Massari D., Veljanoski J., Brown A. G. A., 2018, *Nature*, **563**, 85
- Hernquist L., 1990, *ApJ*, **356**, 359
- Ibata R., Lewis G. F., Irwin M., Totten E., Quinn T., 2001, *ApJ*, **551**, 294
- Ibata R. A., Lewis G. F., Irwin M. J., Cambr esy L., 2002, *MNRAS*, **332**, 921
- Ibata R. A., et al., 2017a, *ApJ*, **848**, 128
- Ibata R. A., et al., 2017b, *ApJ*, **848**, 129
- Ibata R. A., Malhan K., Martin N. F., 2019, *ApJ*, **872**, 152
- Ibata R., et al., 2020, arXiv e-prints, p. [arXiv:2012.05245](https://arxiv.org/abs/2012.05245)
- Johnston K. V., Hernquist L., Bolte M., 1996, *ApJ*, **465**, 278
- Johnston K. V., Bullock J. S., Sharma S., Font A., Robertson B. E., Leitner S. N., 2008, *ApJ*, **689**, 936
- Juri c M., et al., 2008, *ApJ*, **673**, 864
- King I., 1962, *AJ*, **67**, 471
- Kundu R., Minniti D., Singh H. P., 2019, *MNRAS*, **483**, 1737
- K upper A. H. W., Balbinot E., Bonaca A., Johnston K. V., Hogg D. W., Kroupa P., Santiago B. X., 2015, *ApJ*, **803**, 80
- Lamb M. P., Venn K. A., Shetrone M. D., Sakari C. M., Pritzl B. J., 2015, *MNRAS*, **448**, 42
- Laureijs R., et al., 2011, arXiv e-prints, p. [arXiv:1110.3193](https://arxiv.org/abs/1110.3193)
- Lehmann I., Scholz R. D., 1997, *A&A*, **320**, 776
- Leon S., Meylan G., Combes F., 2000, *A&A*, **359**, 907
- Lindegren L., et al., 2018, *A&A*, **616**, A2
- Luo A. L., et al., 2015, *Research in Astronomy and Astrophysics*, **15**, 1095
- Lux H., Read J. I., Lake G., Johnston K. V., 2012, *MNRAS*, **424**, L16
- Mackereth J. T., et al., 2019, *MNRAS*, **482**, 3426
- Majewski S. R., Skrutskie M. F., Weinberg M. D., Ostheimer J. C., 2003, *ApJ*, **599**, 1082
- Malhan K., Ibata R. A., 2018, *MNRAS*, **477**, 4063
- Malhan K., Ibata R. A., 2019, *MNRAS*, **486**, 2995
- Malhan K., Ibata R. A., Martin N. F., 2018, *MNRAS*, **481**, 3442
- Mateu C., Read J. I., Kawata D., 2018, *MNRAS*, **474**, 4112
- McConnachie A. W., et al., 2018, *ApJ*, **868**, 55
- Miyamoto M., Nagai R., 1975, Publications of the Astronomical Society of Japan, **27**, 533
- Moreno E., Pichardo B., Vel azquez H., 2014, *ApJ*, **793**, 110
- Navarro J. F., Frenk C. S., White S. D. M., 1996, *ApJ*, **462**, 563
- Necib L., Ostdiek B., Lisanti M., Cohen T., Freytsis M., Garrison-Kimmel S., 2019, arXiv e-prints, p. [arXiv:1907.07681](https://arxiv.org/abs/1907.07681)
- Necib L., et al., 2020, *Nature Astronomy*,
- Odenkirchen M., Grebel E. K., 2004, in Prada F., Martinez Delgado D., Mahoney T. J., eds, Astronomical Society of the Pacific Conference Series Vol. 327, Satellites and Tidal Streams. p. 284 ([arXiv:astro-ph/0307481](https://arxiv.org/abs/astro-ph/0307481))
- Oliver W. H., Elahi P. J., Lewis G. F., Power C., 2020, arXiv e-prints, p. [arXiv:2012.04823](https://arxiv.org/abs/2012.04823)
- Pearson S., K upper A. H. W., Johnston K. V., Price-Whelan A. M., 2015, *ApJ*, **799**, 28
- Plummer H. C., 1911, *MNRAS*, **71**, 460
- Powell D., 2013, *Nature*, **502**, 22
- Price-Whelan A. M., 2017, *The Journal of Open Source Software*, **2**, 388
- Pryor C., McClure R. D., Fletcher J. M., Hesser J. E., 1991, *AJ*, **102**, 1026
- Racca G. D., et al., 2016, in MacEwen H. A., Fazio G. G., Lystrup M., Batalha N., Siegler N., Tong E. C., eds, Society of Photo-Optical Instrumentation Engineers (SPIE) Conference Series Vol. 9904, Space Telescopes and Instrumentation 2016: Optical, Infrared, and Millimeter Wave. p. 99040O ([arXiv:1610.05508](https://arxiv.org/abs/1610.05508)), [doi:10.1117/12.2230762](https://doi.org/10.1117/12.2230762)
- Sans Fuentes S. A., De Ridder J., Deboscher J., 2017, *A&A*, **599**, A143
- Sch onrich R., Binney J., Dehnen W., 2010, *MNRAS*, **403**, 1829
- Searle L., Zinn R., 1978, *ApJ*, **225**, 357
- Sollima A., 2020, *MNRAS*, **495**, 2222
- The Dark Energy Survey Collaboration 2005, arXiv e-prints, [pp astro-ph/0510346](https://arxiv.org/abs/astro-ph/0510346)
- Thomas G. F., Famaey B., Ibata R., L ughausen F., Kroupa P., 2017, *A&A*, **603**, A65
- Thomas G. F., et al., 2018a, *MNRAS*, **481**, 5223
- Thomas G. F., Famaey B., Ibata R., Renaud F., Martin N. F., Kroupa P., 2018b, *A&A*, **609**, A44
- Thomas G. F., et al., 2019, *ApJ*, **886**, 10
- Thomas G. F., et al., 2020, arXiv e-prints, p. [arXiv:2009.04487](https://arxiv.org/abs/2009.04487)
- Venn K. A., Tolstoy E., Kaufer A., Kudritzki R. P., 2004, in McWilliam A., Rauch M., eds, Origin and Evolution of the Elements. p. 58 ([arXiv:astro-ph/0305188](https://arxiv.org/abs/astro-ph/0305188))
- White S. D. M., Rees M. J., 1978, *MNRAS*, **183**, 341
- York D. G., et al., 2000, *AJ*, **120**, 1579

This paper has been typeset from a $\text{\TeX}/\text{\LaTeX}$ file prepared by the author.